Friedel oscillations at the Dirac cone merging point in anisotropic graphene and graphenelike materials

Clément Dutreix,[1] Liviu Bilteanu,[1] Anu Jagannathan,[1] and Cristina Bena[1,2]
[1]*Laboratoire de Physique des Solides, CNRS UMR-8502, Université Paris Sud, 91405 Orsay Cedex, France*
[2]*Institute de Physique Théorique, CEA/Saclay, Orme des Merisiers, 91190 Gif-sur-Yvette Cedex, France*
(Received 26 October 2012; revised manuscript received 19 February 2013; published 10 June 2013)

We study the Friedel oscillations induced by a localized impurity in an anisotropic graphenelike structure. We focus on the limit when the two inequivalent Dirac points merge. We find that, in this limit, the Friedel oscillations manifest very peculiar features, such as a strong asymmetry and an atypical inverse square-root decay. Our calculations are performed using both a T-matrix approximation and a tight-binding exact diagonalization technique. They allow us to numerically obtain the local density of states as a function of energy and position as well as an analytical form of the Friedel oscillations in the continuum limit. The two techniques yield results that are in excellent agreement, confirming the accuracy of such methods to approach this problem.

DOI: 10.1103/PhysRevB.87.245413 PACS number(s): 71.23.An

I. INTRODUCTION

Graphene has known an increased interest over the past few years with some of the most interesting questions, at present, focusing on the possibility to modify the electronic structure of graphene, either by mechanical deformations, such as stretching[1] or twisting[2,3] via chemical additions or by changing the nature of the substrate. In light of possible important applications, the most promising directions have been towards opening a gap,[4] enhancing the spin-orbit interaction, the realization of the quantum spin Hall effect,[4–7] and obtaining quantum Hall states using pseudomagnetic (curvature) fields.[8,9]

One of the most studied modifications of graphene is mechanical stretching, which gives rise to a hopping anisotropy and, consequently, to a strong renormalization of the band structure. Such hopping anisotropies can yield interesting modifications of the band structure, for example, a critical value of the anisotropy is expected to give rise to a hybrid Dirac cone, exhibiting a linear dispersion along one direction and a quadratic one along the perpendicular one.[1] Although such anisotropy is not experimentally achievable via mechanical stretching, recently, the realization of a cold-atom equivalent of such an anisotropic system has been achieved.[10] Similar hybrid Dirac cones have been predicted to arise when the higher-order hopping parameters are strongly enhanced,[11,12] which may occur, for example, in the presence of adatoms. In the future, one can hope that this could be engineered as well in graphenelike hexagonal molecular structures, such as the one described in Ref. 13.

In this paper, we focus on a system with such hybrid semi-Dirac points, and we study the Friedel oscillations (FOs) generated in the presence of a single localized impurity. We use both analytical techniques, such as the T-matrix approximation, and numerical techniques (the exact diagonalization of the lattice tight-binding Hamiltonian). Using the T-matrix approximation, we obtain the form of the Fourier transform of the Friedel oscillations induced by the impurity. We also calculate the real-space form of these oscillations. For small energies and long distances (in the continuum limit), we obtain an exact analytical form of these oscillations, whereas, we evaluate the short distance behavior of the Friedel oscillations using a numerical integration. On the other hand, we calculate the local density of states (LDOS) at each lattice site using an exact diagonalization of the lattice tight-binding Hamiltonian. Finally, we study the form of the LDOS at zero energy using wave-function arguments along the lines of Ref. 14, which allow us to obtain an analytical form for the impurity state at zero energy. The results obtained via the above methods are in perfect agreement, confirming the accuracy of these tools for describing the impurity effects in such systems.

The most interesting characteristic of the observed Friedel oscillations is a strong anisotropic spatial dependence—the period and decay length of these oscillations depends strongly on direction—consistent with the anisotropy of the band structure. Also, we observe an atypical inverse square-root decay for long distances and small energies on each of the two A and B sublattices. Moreover, similar to the isotropic graphene, the LDOS contributions of the two sublattices are dephased by π, yielding a cancellation of the $1/\sqrt{r}$ terms and an effective $1/r$ decay of these oscillations with the distance from the impurity.

The structure of the paper is as follows. In Sec. II, we present the model employed to describe isotropic as well as anisotropic graphene. In Sec. III, we present the Friedel oscillations in the LDOS calculated using wave-function considerations (Sec. III A), tight-binding exact diagonalization (Sec. III B), and the T-matrix approximation (Sec. III C). We conclude in Sec. IV.

II. MODEL

Graphene consists of a honeycomb lattice of carbon atoms with two atoms (A and B) per unit cell (see Fig. 1). Denoting the distance between two nearest neighbors a_0 with $a_0 = 0.142$ nm, then $\mathbf{a}_1 = a_0(-\frac{\sqrt{3}}{2}, \frac{3}{2})$ and $\mathbf{a}_2 = a_0(\frac{\sqrt{3}}{2}, \frac{3}{2})$ are basis vectors of the triangular Bravais lattice.

The corresponding first Brillouin zone (BZ) is hexagonal as depicted by the green dashed line in Fig. 2. Its geometrical properties only depend on the Bravais lattice. Nevertheless, the number of atoms per unit cell becomes relevant for the energy spectrum. For graphene (two atoms per unit cell with one electron per atom), the energy bands are well described using

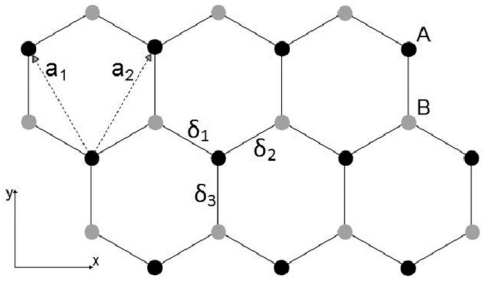

FIG. 1. Graphene honeycomb lattice.

a tight-binding model: Each $2p_z$ electron may hop between two sites i and j with a given amplitude t_{ij}. In this paper, we only consider the hopping between nearest neighbors with a fixed hopping amplitude $t \approx 2.7$ eV for the nearest-neighbor vectors $\vec{\delta}_1$, $\vec{\delta}_2$, and a variable amplitude t' for $\vec{\delta}_3$. The corresponding second-quantized Hamiltonian is given by

$$\mathcal{H} = \sum_{\langle i,j \rangle} t_{ij} a_i^\dagger b_j + \text{H.c.} \tag{1}$$

$$= \int_{\text{BZ}} \frac{d^2k}{S_{\text{BZ}}} [a^\dagger(\vec{k}), b^\dagger(\vec{k})] \mathcal{H}_{\vec{k}} \begin{pmatrix} a(\vec{k}) \\ b(\vec{k}) \end{pmatrix}, \tag{2}$$

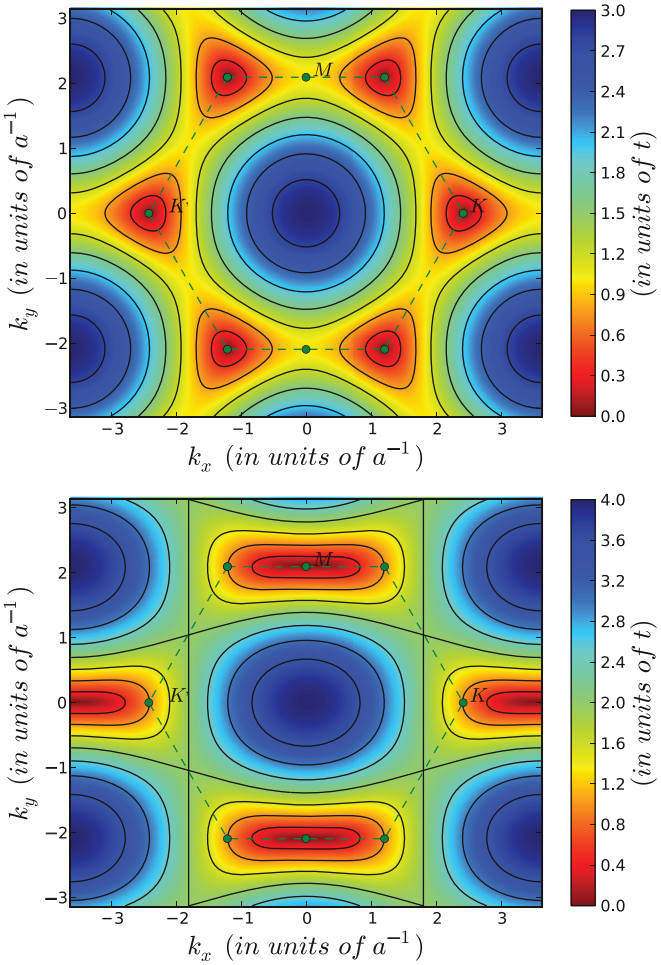

FIG. 2. (Color online) Energy spectra when $t' = t$ (top) and $t' = 2t$ (bottom). The latter corresponds to the merging of Dirac points into a single point M. The green dashed line depicts the Brillouin zone.

with $\mathcal{H}_{\vec{k}} = \begin{pmatrix} 0 & f(\vec{k}) \\ f^*(\vec{k}) & 0 \end{pmatrix}$ and $f(\vec{k}) = -t(e^{-i\vec{k}\cdot\vec{\delta}_1} + e^{-i\vec{k}\cdot\vec{\delta}_2}) - t'e^{-i\vec{k}\cdot\vec{\delta}_3}$. S_{BZ} is the area of the BZ. The operators a (b) and $a^\dagger$ ($b^\dagger$) are field operators that annihilate and create, respectively, an electron on the $A(B)$ sublattice. The energy spectrum is then obtained by diagonalizing the Hamiltonian matrix $\mathcal{H}_{\vec{k}}$. As there are two atoms per unit cell, there are two energy bands $\epsilon_\pm(\vec{k}) = \pm|f(\vec{k})|$. Negative values of ϵ correspond to the valence band, whereas, positive ones correspond to the conduction band. When $t' = t$, there are two inequivalent points K and K' at the corners of the BZ for which the two bands touch. These points are denoted Dirac points since the energy spectrum is conical in their vicinity. Note that the coincidence between the Dirac points (determined by the band structure) and that of the corners of the BZ (intrinsic to the Bravais lattice) occurs only when $t' = t$ as mentioned in Refs. 1, 11, and 12.

Figure 2 illustrates the fact that the Dirac points move away from the corners of the BZ when varying the hopping parameter t'. Increasing this amplitude from t to $2t$ makes the two inequivalent Dirac points merge[11,12] at the M point (right at the middle of the edges of the BZ). The critical value $t' = 2t$ corresponds to the annihilation of a pair of Dirac points with opposite Berry phases. This topological invariant changes abruptly from $\pm\pi$ to 0 at the merging, which, thus, defines a topological transition between a semimetallic phase and a band insulator since a gap opens at the M point for $t' > 2t$. This can be seen by expanding $f(\vec{k})$ in the vicinity of this point defined by $(0, \frac{2\pi}{3a})$

$$f^M(\vec{q}) = \left(\Delta + ic_y q_y + \frac{q_x^2}{2m^*}\right) e^{-i(\pi/3)}. \tag{3}$$

Here, $c_y = 3ta_0$, $2m^* = \frac{4}{3ta_0^2}$, and $\Delta = t' - 2t$ characterizes the distance from the topological transition and gives the value of the gap when $t' > 2t$. Exactly at the transition ($\Delta = 0$), the Hamiltonian exhibits a semi-Dirac energy dispersion such that $\epsilon_\pm^M(\vec{q}) = \pm|f^M(q)|$ is linear in q_y but quadratic with respect to q_x,

$$\epsilon_\pm^M(\vec{q}) = \pm\sqrt{(c_y q_y)^2 + \left(\frac{q_x^2}{2m^*}\right)^2}. \tag{4}$$

III. LOCAL DENSITY OF STATES IN THE PRESENCE OF IMPURITY SCATTERING

The effects of impurity scattering on the graphene LDOS have been extensively studied[15,16] in the past. It has been shown[17–19] that this gives rise to long-wavelength oscillations that decay as $1/r^2$, instead of the $1/r$ law expected for conventional two-dimensional materials. Here, we investigate how the merging of the two Dirac cones changes the form of these long-wavelength oscillations. We start this section with some zero-energy wave-function arguments along the lines of Ref. 14 that allow us to characterize the impurity state. Furthermore, we perform a more detailed study using analytical (T-matrix approximation) and numerical (tight-binding) techniques.

A. Wave-function considerations

1. The sublattice symmetry

A graphene honeycomb lattice contains two atoms per unit cell (A and B), which allows one to define two sublattices. Moreover, the Hamiltonian (1) only takes into account nearest-neighbor hopping processes and neglects hopping between sites belonging to the same sublattice, resulting in a bipartite system. For such systems, a generic Hamiltonian takes the form

$$\mathcal{H} = \begin{pmatrix} 0 & T \\ T^\dagger & 0 \end{pmatrix}. \tag{5}$$

Without loss of generality, T is a $N_A \times N_B$ block (not necessarily a square matrix), where $N_{A(B)}$ is the number of atoms in the $A(B)$ sublattice, assuming there is only one electron per atom. Here, we restrict ourself to $N_B \geqslant N_A$. Such a Hamiltonian anticommutes with

$$\mathcal{S} = \begin{pmatrix} \mathbb{I}_{N_A} & 0 \\ 0 & -\mathbb{I}_{N_B} \end{pmatrix}. \tag{6}$$

$\mathbb{I}_N$ is the $N \times N$ identity matrix so that the unitary operator $\mathcal{S}$ always squares to $+1$, which defines a chiral symmetry: the sublattice symmetry.

This fundamental symmetry implies a particle-hole symmetric spectrum and includes the possibility for the existence of zero-energy states, which transform into themselves under the transformation $\mathcal{S}$. As a consequence, they have null components on one sublattice.

Moreover, as pointed out in Refs. 20–23, every finite bipartite lattice has an extra number of $N_B - N_A$ zero-energy eigenstates living on the sublattice B, regardless of the components of the block T. This is because the non-zero-energy eigenstates appear in pairs: $|\psi\rangle$ and $\mathcal{S}|\psi\rangle$, and in order to form non-zero-energy states, it is necessary to pair a localized state living on the sublattice A with another one living on B. As a number of $N_B - N_A$ zero modes living on the sublattice B are unable to satisfy this condition, they are stuck at zero energy, cannot hybridize to A states, and remain localized purely on B.

2. Zero-energy impurity wave function

In the presence of a single vacancy, $N_B - N_A = 1$, and we have a single zero-mode impurity-state wave function. Here, the fundamental point is that varying parameter t' does not change the structure of the matrix (5). Then, the sublattice symmetry ensures that such a zero mode does exist, even in the gapped phase ($t' > 2$). As a consequence, this zero-energy state is a good candidate to characterize the Dirac cones merging in real space. In this section, we study the form of its wave function, using simple arguments along the lines of Ref. 14. We already know that such a wave function has null components on the A sites, represented by the black disks in Fig. 3, and we need to determine its value on the B sublattice. In Ref. 14, the authors have determined the exact analytic form of the impurity wave function for an isotropic honeycomb lattice with a single vacancy. Their method consists of an appropriate matching of the zero modes of two semi-infinite and complementary graphene sheets. This is the method we generalize in what follows for anisotropic graphene.

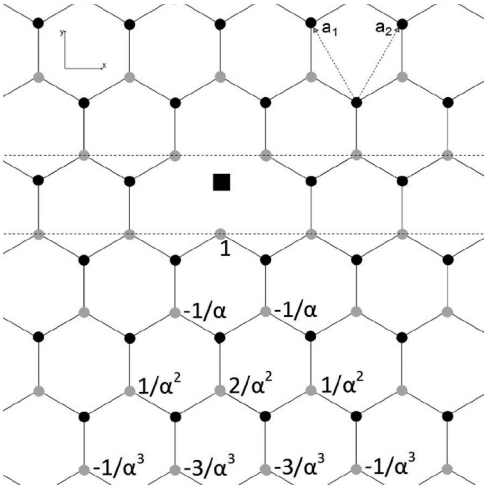

FIG. 3. The zero-energy wave function components for $t' = \alpha t$ with $\alpha \geqslant 2$. The wave function is zero for all sites for which no value is specified. The black square denotes the vacancy. The direction of anisotropy is the y direction. The two dashed lines are the boundaries of the upper and lower half planes, respectively.

In Fig. 3, the two semi-infinite graphene sheets are defined such that their edges are orthogonal to the anisotropic direction, along which $t' = \alpha t$ with $\alpha \geqslant 2$. Here, we have introduced an anisotropy parameter α ($\alpha = 2$ exactly at the merging), that allows us to explore the gapped phase beyond the merging point. The upper half plane has a "bearded" edge (as indicated by the upper dashed line in Fig. 3), whereas, the lower half plane has a zigzag edge.

Let us first consider the lower half plane terminated by the zigzag edge. The form of the edge states for a semi-infinite zigzag ribbon is well known[24,25] for isotropic graphene. In a manner similar to that of Ref. 24, the edge states for anisotropic graphene can be determined by imposing the condition $|2\cos(k/2)| \leqslant \alpha$, where k is the momentum along the edge. Although, for isotropic graphene ($\alpha = 1$), this condition is verified for $2\pi/3 \leqslant k \leqslant 4\pi/3$, above the merging point ($\alpha \geqslant 2$), such a condition is satisfied for all values of k, $0 \leqslant k \leqslant 2\pi$. Next, regarding the complementary semi-infinite bearded plane, the condition becomes $|2\cos(k/2)| \geqslant \alpha$, which cannot be satisfied for any k when $\alpha > 2$. The case of $\alpha = 2$ leads to $k = 0$, associated with an extended state, and there are no allowed edge states in this limit.

The condition that the impurity wave functions on the two semi-infinite planes match at the interface can be written as

$$\alpha b^{(l)}_{m,0} + b^{(u)}_{m,0} + b^{(u)}_{m+1,0} = 0, \tag{7}$$

where $b^{(l)}_{m,n}$ ($b^{(u)}_{m,n}$) corresponds to a given site of the lower (upper) half plane characterized by $\vec{r}_{m,n} = m(\vec{a}_2 - \vec{a}_1) - n\vec{a}_1$. The origin is defined to be on the B atom right below the vacancy in Fig. 3. The above relation is valid everywhere on the edges except for $m = 0$. Introducing $b_{m,0} = \sum_k b_{k,0} e^{ikm}$, the condition (7) can be rewritten in terms of momentum as

$$\alpha \sum_k b^{(l)}_{k,0} e^{ikm} + \sum_{k'} b^{(u)}_{k',0}(1 + e^{ik'}) e^{ik'm} = 0. \tag{8}$$

A possible solution for the boundary conditions is $b^{(l)}_{k,0} = 1$ with $0 \leqslant k \leqslant 2\pi$ and $b^{(u)}_{k',0} = 0$. As for the case of isotropic

graphene studied in Ref. 14, this corresponds to the edge solutions for two isolated complementary semi-infinite planes. Considering the lattice as infinite, the discrete sum in (8) turns into an integral, and the impurity wave function can be written as

$$b^{(l)}_{m,n} \sim \int_0^{2\pi} dk(-2/\alpha)^n \cos^n(k/2)e^{ik(m+n/2)} \sim (-1)^n \frac{\exp\left[-nln\left(\frac{\alpha}{2}\right) - \frac{(2m+n)^2}{2n}\right]}{\sqrt{n}}. \quad (9)$$

The details of the derivation of the above result are presented in Appendix A. This approximation is valid for $\alpha \geqslant 2$ and for long distances. We have defined $x = a_0\sqrt{3}(2m+n)/2$ and $y = -n3a_0/2$. Most useful to compare with the results of the subsequent sections is the behavior of the wave function along the direction $x = 0$. Along this direction, the zero-energy impurity state exhibits an exponential decay with the distance from the impurity in the gapped phase ($\alpha > 2$), whereas, it decays as $1/\sqrt{y}$ at the merging ($\alpha = 2$). As detailed in Appendix A, we check that, in the semimetallic phase (for $1 < \alpha < 2$), the wave function decays as $1/r$ in both directions, albeit exhibiting a strong asymmetry between x and y; we also check that, for $\alpha = 1$, the classical results for the Friedel oscillations in graphene are correctly retrieved. Hence, the decay law of the zero-energy impurity states provides a real-space signature of the Dirac cone merging.

Furthermore, we can evaluate the amplitude of this impurity state by hand, see Fig. 3, by searching for a decaying wave function with null components everywhere in the semi-infinite bearded ribbon. The condition (7) becomes $\alpha b^{(l)}_{m,0} + 0 + 0 = 0$ and must be satisfied at each A site between the two dashed lines, except for the impurity site. So the wave function has zero components along the zigzag edge, except at the site situated right under the impurity for which we take $b^{(l)}_{0,0} = 1$. Then, the Hamiltonian (5) implies that $\alpha b^{(l)}_{m,1} + b^{(l)}_{m,0} + b^{(l)}_{m+1,0} = 0$ for all values of m. This leads to $b^{(l)}_{-1,1} = b^{(l)}_{0,1} = -1/\alpha$ and $b^{(l)}_{m,1} = 0$ for all other sites with $n = 1$. If we extend this analysis to the subsequent rows, we obtain the impurity wave-function values shown in Fig. 3. So, above the merging point, this peculiar localized state describes electrons that are localized only in the lower-half plane of the graphene sheet with a single impurity.

B. Exact diagonalization

In order to obtain the local density of states on the lattice in the presence of disorder, one can diagonalize exactly or, using numerical approximation, the lattice tight-binding Hamiltonian. Here, since the systems we consider are not too large (around 1800 atoms), we base ourselves on an exact diagonalization technique. The lattice Hamiltonian is defined by

$$\mathcal{H} = -\sum_{\langle i,j\rangle} t_{ij}|i\rangle\langle j| + V_0|0\rangle\langle 0|, \quad (10)$$

where $|i\rangle$ stands for the $2p_z$ nonhybridized orbital centered on site i. The impurity that we consider is a vacancy, which can be modeled by removing the corresponding atom from the lattice or by taking an infinite value for V_0. By $|k\rangle$, we denote the eigenstate corresponding to the eigenvalue E_k. The eigenfunctions of (10) can be written as a linear combination of individual orbitals,

$$|k\rangle = \sum_i c_{ki}|i\rangle, \quad (11)$$

$$c_{ki} = \langle i|k\rangle, \quad (12)$$

The LDOS, corresponding to the number of available states on a site i at energy E, is then given by

$$\rho_i(E) = \sum_k |c_{ki}|^2 f_k(E), \quad (13)$$

where $f_k(E) = \delta(E - E_k)$ is the Dirac δ function centered on the eigenenergy E_k. Although, in an infinite system, this procedure automatically yields a continuous energy spectrum, in a finite sample, the spectrum is smoothed by taking f_k to be a Gaussian or a Lorentzian.

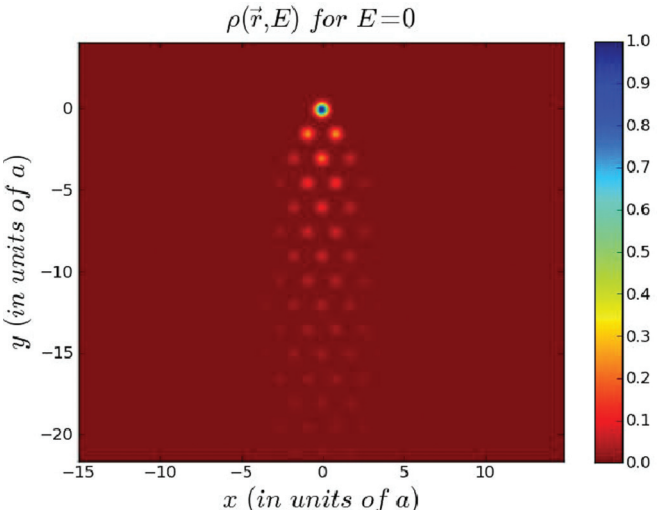

FIG. 4. (Color online) Snapshot of the LDOS obtained using exact diagonalization. We plot the zero-energy impurity state slightly above the merging point ($\alpha = 2.1$) when a small gap opens in the spectrum. The highest-intensity site (in blue) corresponds to the B site right below the impurity.

In Fig. 4, we show the LDOS obtained using this method at zero energy in the gapped phase ($\alpha = 2.1$). This is in agreement with the zero-energy wave function described previously and depicted in Fig. 3. The result for the spatial dependence of the LDOS at a finite energy is presented in Fig. 7. Note the strong asymmetry of the LDOS between the positive and the negative values of y close to the impurity. Although some of these features are consistent with the previous observations concerning the impurity-state wave functions, we also investigate them in more detail (for example, in what concerns their energy dependence) in the next section via the T-matrix approximation technique.

C. T-matrix approximation

The T-matrix approximation consists of a perturbative expansion of the Green's function to all orders in the impurity scattering as shown in Fig. 5. In this paper, we consider the case of a localized impurity $V(\vec{r}) = V_0\delta(\vec{r})$ situated on a sublattice A for which $V(q)$ is independent of momentum. Moreover,

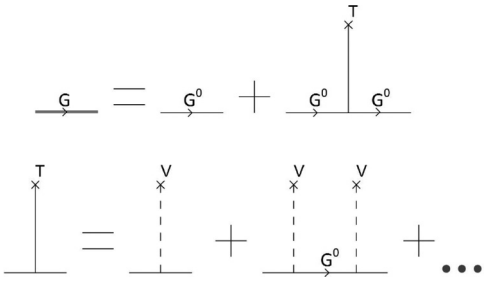

FIG. 5. Diagrammatic perturbative expansion of the generalized Green's function to all orders in the impurity potential.

here, the impurity refers to a vacancy for which V_0 becomes infinite.

The expansion of the T matrix in Fig. 5 is a geometric series, and the infinite summation of diagrams can be performed exactly

$$T(i\omega_n) = \left[I_2 - V \int_{\mathrm{BZ}} \frac{d^2k}{S_{\mathrm{BZ}}} G_0(\vec{k}, i\omega_n) \right]^{-1} V, \qquad (14)$$

where S_{BZ} is the area of the BZ, $i\omega_n$ is a Matsubara frequency, $G_0(\vec{k}, i\omega_n) = [i\omega_n I_2 - \mathcal{H}_{\vec{k}}]^{-1}$ is the unperturbed Green's function, I_2 is the 2×2 identity matrix, and $V = \left(\begin{smallmatrix} V_0 & 0 \\ 0 & 0 \end{smallmatrix}\right)$.

We define $\Delta\rho$ as the correction to the LDOS due to the impurity. According to Fig. 5, we have

$$\begin{aligned} \Delta G(\vec{R}_i, \vec{R}_j, E) &\doteq G(\vec{R}_i, \vec{R}_j, E) - G^0(\vec{R}_i - \vec{R}_j, E) \\ &= G^0(\vec{R}_i, E) T(E) G^0(-\vec{R}_j, E). \end{aligned} \qquad (15)$$

The correspondence between the components of ΔG in the continuum and on the lattice is the following:

$$\begin{aligned} \Delta G_{\alpha\beta}(\vec{r}_1, \vec{r}_2, E) = \sum_{i,j} & \phi_\beta(\vec{r}_1 - \vec{R}_j) \phi^*_\alpha(\vec{r}_2 - \vec{R}_i) \\ & \times \Delta G_{\alpha\beta}(R_j, R_i, E), \end{aligned} \qquad (16)$$

where $\phi_{\alpha(/\beta)}$ is a carbon $2p_z$ orbital and the α and β indices denote the sublattice, whereas, i and j label the unit cell. The impurity correction to the LDOS is given by

$$\Delta\rho(\vec{r}, E) = -\frac{1}{\pi} \mathrm{Im}[\mathrm{Tr}\{\Delta G(\vec{r}, \vec{r}, E)\}], \qquad (17)$$

which yields in the momentum space,

$$\begin{aligned} \Delta\rho(\vec{q}, E) = \frac{i}{2\pi} \int_{\mathrm{BZ}} \frac{d^2k}{S_{\mathrm{BZ}}} \mathrm{Tr}\{ & \Delta G(\vec{k} + \vec{q}, \vec{k}, E) \\ & - \Delta G^*(\vec{k}, \vec{k} + \vec{q}, E)\}. \end{aligned} \qquad (18)$$

1. Momentum dependence of the Fourier transform of the LDOS

We focus first on the evaluation of the momentum dependence of $\Delta\rho$, corresponding to the measured Fourier transform of the LDOS. In Fig. 6, we plot this momentum dependence for $\omega = 0.15t$ and $\omega = 0.8t$. The first column corresponds to isotropic graphene ($t' = t$). As noted previously,[19] the central circle (in red) corresponds to intranodal scattering, whereas, the outer regions around the corners of the BZ correspond to internodal scattering. In the second column, we consider an intermediate value of $t' = 1.5t$, whereas, in the third column, we consider the Dirac cone merging limit $t' = 2t$. We note that the outer regions disappear at the merging point for which internodal quasiparticle scattering no longer exists. Moreover, we note that the features corresponding to intranodal scattering, centered on the sites of the reciprocal lattice, are strongly anisotropic, corresponding to the low-energy anisotropic semi-Dirac spectrum.

2. Friedel oscillations in real space

In what follows, we focus on the real-space form of the Friedel oscillations. Although they can be evaluated numerically for arbitrary energy and position using the formulas presented in the previous section, we can also obtain an analytical form of these oscillations in certain limits by performing an expansion of the Hamiltonian at low energies. In what follows, we exclusively focus on the merging point corresponding to $t' = 2t$ in the considered model so that the low-energy physics is dominated by the semi-Dirac spectrum around the M point.

Using the expansion (3) with $\Delta = 0$, the unperturbed Green's function for $x = 0$ can be rewritten as

$$G^0(0, y, \omega) = \begin{pmatrix} G^0_{AA}(0, y, \omega) & G^0_{AB}(0, y, \omega) \\ G^0_{BA}(0, y, \omega) & G^0_{BB}(0, y, \omega) \end{pmatrix}, \qquad (19)$$

with

$$\begin{aligned} G^0_{AA}(0, y, \omega) &= -i 2^{-5/4} \pi^{3/2} \Gamma(1/4) \omega^{-1/4} y^{1/4} H^{(1)}_{-1/4}(\omega y), \\ G^0_{BB}(0, y, \omega) &= G_{AA}(0, y, \omega), \\ G^0_{AB}(0, y, \omega) &= -i A 2^{-3/4} \pi^{3/2} \Gamma(3/4) \omega^{1/4} y^{-1/4} H^{(1)}_{1/4}(\omega y) \\ &\quad \mp i A i 2^{-5/4} \pi^{3/2} \Gamma(1/4) \omega^{3/4} y^{1/4} H^{(1)}_{3/4}(\omega y), \\ G^0_{BA}(0, y, \omega) &= -i \bar{A} 2^{-3/4} \pi^{3/2} \Gamma(3/4) \omega^{1/4} y^{-1/4} H^{(1)}_{1/4}(\omega y) \\ &\quad \mp i \bar{A} i 2^{-5/4} \pi^{3/2} \Gamma(1/4) \omega^{3/4} y^{1/4} H^{(1)}_{3/4}(\omega y), \end{aligned} \qquad (20)$$

where $H^{(1)}_\nu$ are Hankel functions of the first kind, Γ is the Euler γ function, and $\bar{A}$ is the conjugate of an arbitrary phase factor A that depends on the basis we choose to write as $f(\vec{k})$; the value of any observable physical quantity should be independent of this choice.[26] Note that, on the right-hand side of the above formulas, we have chosen to denote the absolute value $|y|$ simply by y. Moreover, the $\mp$ signs correspond to a positive and negative value, respectively, for y. The antisymmetric form of G_{AB} and G_{BA} is responsible for an anisotropy of the impurity-induced corrections to the LDOS on the B sublattice as will be described in more detail in what follows. According to Eq. (17), the LDOS correction on each sublattice is given by

$$\begin{aligned} \Delta\rho_{AA}(0, y, \omega) &= -\frac{1}{\pi} \mathrm{Im}\left[G^0_{AA}(0, y, \omega) t(\omega) G^0_{AA}(0, -y, \omega) \right], \\ \Delta\rho_{BB}(0, y, \omega) &= -\frac{1}{\pi} \mathrm{Im}\left[G^0_{BA}(0, y, \omega) t(\omega) G^0_{AB}(0, -y, \omega) \right], \end{aligned} \qquad (21)$$

where $t(\omega)$ is the only non-nul component of the T matrix. In the case of an infinite impurity potential (vacancy), it takes the

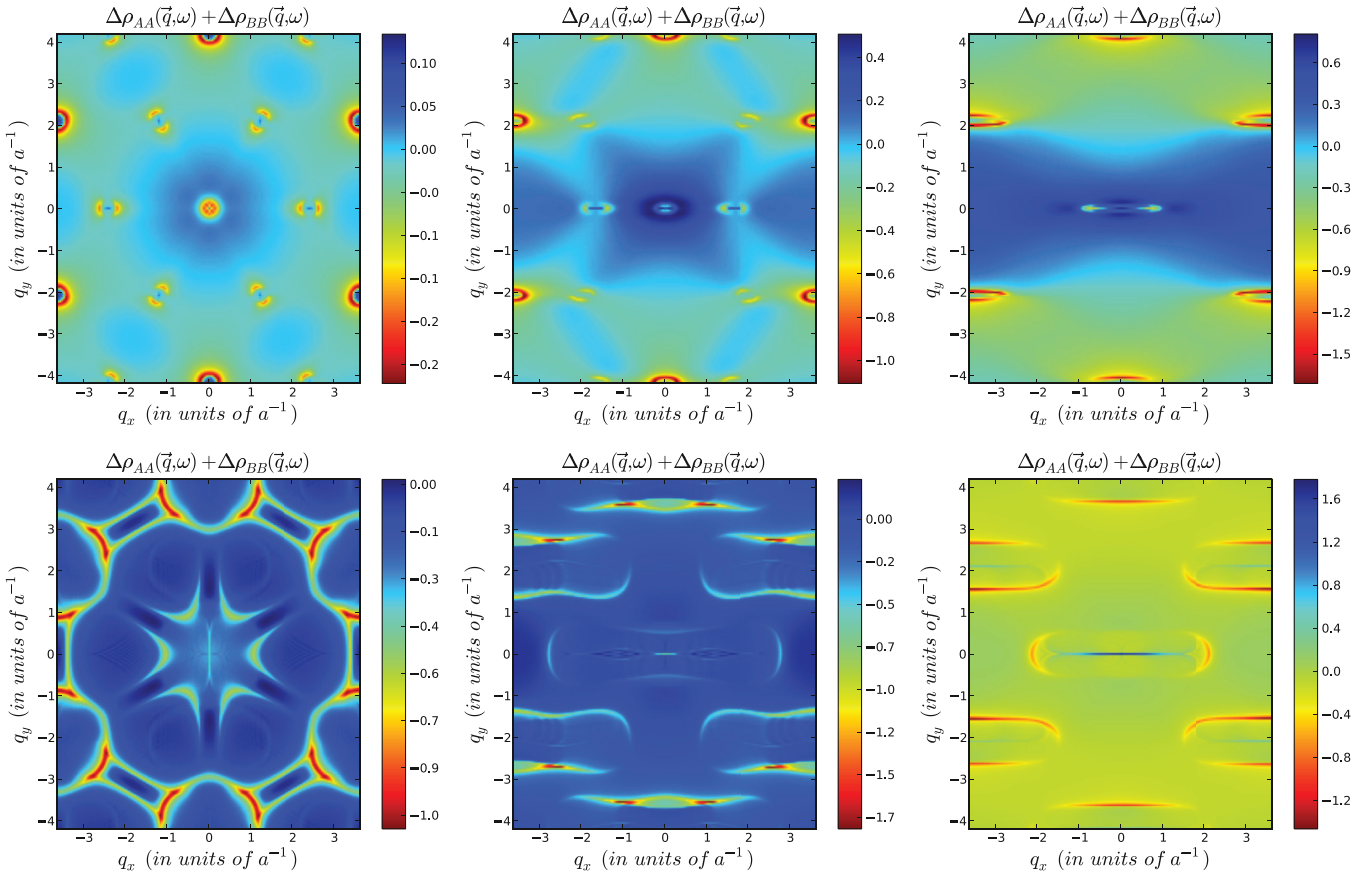

FIG. 6. (Color online) Fourier transform of the LDOS correction $\Delta\rho$ when $t' = t$ (first column), $t' = 1.5t$ (second column), and $t' = 2t$ (third column). The energy is $\omega = 0.15t$ for the first row and $\omega = 0.80t$ for the second row.

form

$$t(\omega) \sim \frac{e^{-i\pi/4}}{\omega^{1/2}}. \tag{22}$$

At this point, we can check that, at zero energy, our T-matrix calculations recover the same expression for the LDOS as the one obtained from the zero-energy wave-function considerations. In the limit $\omega \to 0$,

$$G^0_{AA}(0,y,\omega) \sim \omega^{1/2}, \quad G^0_{AB}(0,y,\omega) \sim A\frac{e^{i\pi}}{\sqrt{y}}\theta(y), \tag{23}$$

where θ is the Heaviside step function. The LDOS correction then vanishes on the sublattice A. We stress that the sublattice symmetry implies that, at zero energy, the LDOS on the sublattice A is zero, whereas, it behaves in the following manner on the sublattice B:

$$\Delta\rho_{BB}(0,y,\omega) \sim \frac{\theta(-y)}{\omega^{1/2}y}. \tag{24}$$

This result is in agreement with the analysis of the zero-energy wave function. Remember that the impurity wave function decays as $1/\sqrt{y}$ with the distance from the impurity [cf. (9)], which then leads to a $1/y$ decay for the LDOS.

Now, we turn back to the FOs and evaluate the corrections to the LDOS using the corresponding expressions for the Green's function components in Eq. (20). The results are presented in Fig. 7. We compare these results to a full evaluation of the T matrix (without performing the low-energy expansion) as well as with results obtained using the tight-binding method. As can be seen in Fig. 7, all methods yield very similar results, which confirms their accuracy for this type of calculation. We also note that the LDOS correction is asymmetric between the positive and the negative values of y on the B sublattice, whereas, it is symmetric on the A sublattice.

To obtain the asymptotic expansion of the Friedel oscillations, we expand the Hankel functions for large values of ωy, and we get

$$\begin{aligned}\Delta\rho_{AA}(0,y,\omega) &\sim \frac{1}{y^{1/2}}\cos\left(\frac{2\omega y}{c_y}+\pi\right),\\ \Delta\rho_{BB}(0,y,\omega) &\sim \frac{1}{y^{1/2}}\cos\left(\frac{2\omega y}{c_y}\right).\end{aligned} \tag{25}$$

The resulting FOs decay as $1/\sqrt{y}$ at long distances on both sublattices, slower than the typical inverse decay for a regular two-dimensional system, however, their period is still proportional to $1/\omega$. When summing the contribution of the two sublattices, the terms in $y^{-1/2}$, which are dephased by a factor of π, vanish. The FOs are then described by the next leading correction, which is nonzero only on the B sublattice,

$$\Delta\rho(0,y,\omega) \sim \mp\frac{1}{\omega^{1/2}y}\cos\left(\frac{2\omega y}{c_y}+\frac{\pi}{4}\right). \tag{26}$$

Here, the minus/plus signs correspond to positive and negative values, respectively, of y. The long-wavelength oscillations,

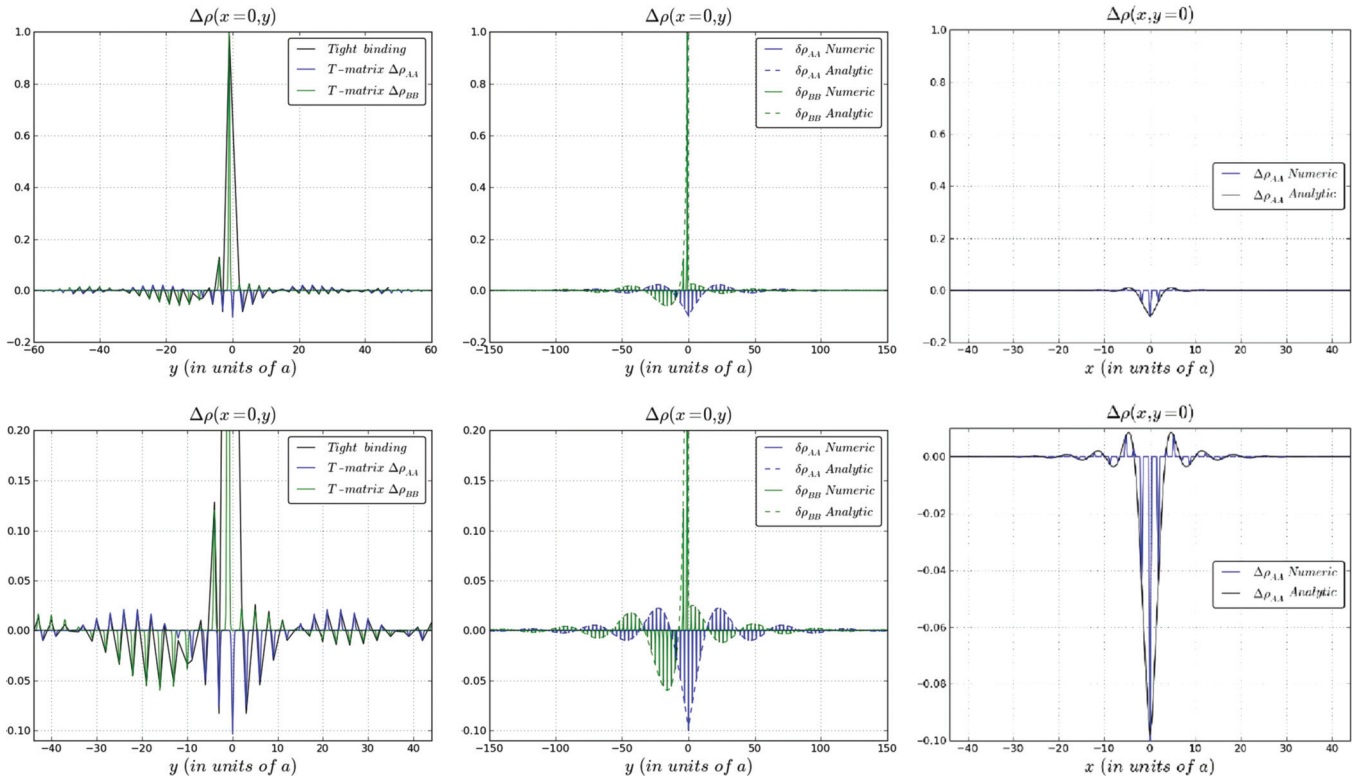

FIG. 7. (Color online) The LDOS correction as a function of position in the vicinity of the impurity for a critical value of anisotropy ($t' = 2t$). The second line presents a series of zoom ins of the plots outlined on the first line. In the first column, we compare $\Delta\rho$ obtained using the full T-matrix approximation to the one obtained by the tight-binding method for an energy $\omega = -0.20t$. Note that, consistent with the low-energy expansion given by Eq. (25), the FOs are dephased by π between the two sublattices. The second column presents a comparison between the correction to the LDOS $\Delta\rho$ along the $x = 0$ direction obtained by the full T-matrix approximation (full lines) and by the low-energy expansion (dotted lines) for $\omega = -0.20t$. In blue, we plot the LDOS on the A sublattice comprising the impurity ($y = 0$), whereas, in green, we plot the LDOS on the B sublattice. In the third column, we plot the LDOS along the $y = 0$ direction obtained by the full T-matrix approximation for $\omega = -0.20t$. The blue curve is obtained using the full T-matrix approximation, whereas, the black one is obtained in the continuum approximation.

thus, decay following the usual $1/y$ law, different from the $1/r^2$ law corresponding to the intranodal scattering in typical graphene. Thus, the transition from the $1/r^2$ decay to a $1/r$ decay in the low-energy FOs provides a real-space signature of the Dirac points merging.

The Friedel oscillations along the perpendicular direction ($y = 0$) cannot be evaluated analytically, however, in the third column of Fig. 7, we plot the dependence of the Friedel oscillations as a function of x for $y = 0$. Note that the amplitude of the oscillations is greatly reduced with respect of the oscillations in the y direction, consistent with the asymmetric shape of the impurity-state cloud, elongated in the y direction.

In Fig. 8, we also present a two-dimensional plot of the LDOS at a finite energy, obtained both by using the full T-matrix form and by using the low-energy expansion. Note that the behavior is very similar to that obtained using the tight-binding method described in the previous section.

So far, the phase beyond the merging point has not been explored. In such a gapped phase, the expansion (3) leads to

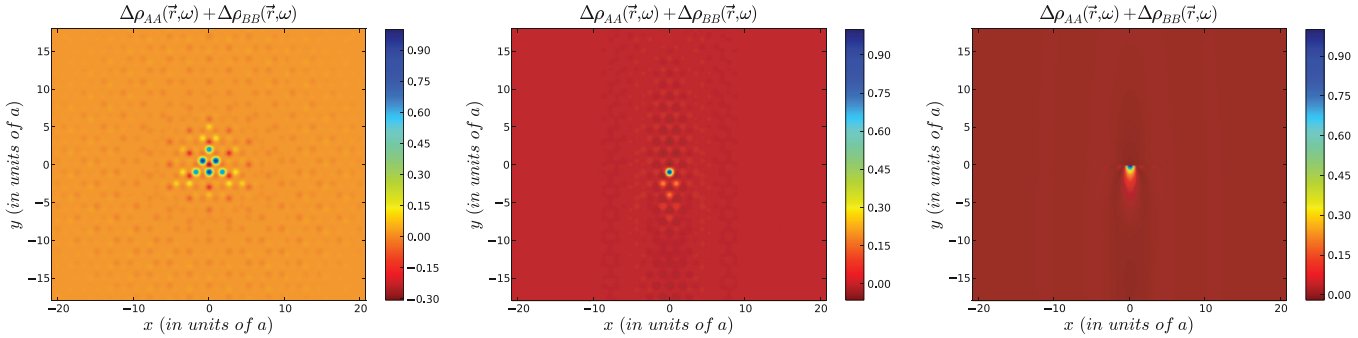

FIG. 8. (Color online) Correction of the LDOS $\Delta\rho$ (in arbitrary units) for $t' = t$ (first column) and $t' = 2t$ (second and third columns), obtained using the full T-matrix approximation (first and second columns) and the low-energy expansion (third column). The energy is $\omega = 0.15t$.

the following spectrum, which is quadratic in both directions, although anisotropic:

$$\epsilon_{\pm}^{M}(\vec{q}) = \pm\left(\Delta + \frac{q_x^2}{2m^*} + \frac{c_y^2 q_y^2}{2\Delta}\right). \tag{27}$$

Defining $X = xm^*/\Delta$ and $Y = y/c_y$ so that $\vec{R} = (X,Y)$ and using expansion (B5), the LDOS correction for electrons in the valence or conduction bands ($\omega^2 > \Delta^2$) can be written as

$$\begin{aligned}\Delta\rho_{AA}(\vec{R},\omega) &\sim \frac{\omega}{|\vec{R}|}\cos(2\sqrt{\omega^2-\Delta^2}|\vec{R}|),\\ \Delta\rho_{BB}(\vec{R},\omega) &\sim \frac{\Delta^2}{\omega|\vec{R}|}\cos(2\sqrt{\omega^2-\Delta^2}|\vec{R}|).\end{aligned} \tag{28}$$

Note that the Friedel oscillations decay as $1/R$ on both sublattices, typical of a usual bidimensional electron gas.

Besides, when $\omega^2 < \Delta^2$, expansion (B5) holds for $\omega \to i\omega$ so that the LDOS decays exponentially with the gap,

$$\begin{aligned}\Delta\rho_{AA}(\vec{R},\omega) &\sim \frac{\omega}{|\vec{R}|}e^{-2\sqrt{\Delta^2-\omega^2}|\vec{R}|},\\ \Delta\rho_{BB}(\vec{R},\omega) &\sim \frac{\Delta^2}{\omega|\vec{R}|}e^{-2\sqrt{\Delta^2-\omega^2}|\vec{R}|}.\end{aligned} \tag{29}$$

IV. CONCLUSION

We have studied the LDOS in the presence of a simple impurity for an anisotropic graphene system at the Dirac cone merging point. We have found that, near this particular point, the zero-energy impurity wave function and the Friedel oscillations in the LDOS exhibit very peculiar features. In particular, the decay length of the Friedel oscillations along the anisotropy direction and along the direction perpendicular to this direction are very different, yielding a very asymmetric impurity state in real space. The spatial dependence of the impurity state wave function allows us to clearly distinguish the semimetallic phase (power-law decay of the wave function with the distance from the impurity) from the gapped phase (exponential decay). On the other hand, the semi-Dirac spectrum near the merging point induces a change in the decay laws in the Friedel oscillations from an inverse-square law ($1/r^2$) below the transition to an inverse-linear law ($1/r$) exactly at the transition. At low energies this provides a real-space signature of the topological transition.

The agreement between the methods that we have used, the analytical T-matrix approximation, the numerical tight-binding exact diagonalization, and the wave-function considerations, is remarkable, proving the accuracy of these methods to describe the LDOS in the presence of disorder in a generic two-dimensional system.

ACKNOWLEDGMENTS

We would like to thank J.-N. Fuchs, F. Piechon, and G. Montambaux for interesting discussions and comments. This work has been supported by the ANR project NANOSIM GRAPHENE under Grant No. ANR-09-NANO-016 and by the FP7 ERC Starting Independent Researcher Grant No. NANO-GRAPHENE 256965.

APPENDIX A: ZERO-ENERGY WAVE-FUNCTION EXPANSION

The general form of Eq. (9) for an arbitrary value of α is

$$\begin{aligned}b_{m,n}^{(l)} &\sim \int_{2A}^{2B} dk(-2/\alpha)^n \cos^n(k/2)e^{ik(m+n/2)}\\ &\sim \int_{A}^{B} 2\,dk(-2/\alpha)^n \cos^n(k)e^{ik(2m+n)}.\end{aligned} \tag{A1}$$

The condition to determine points A and B is $|2\cos(k/2)| = \alpha$, leading to $k/2 = A$ or $k/2 = B = \pi - A$. For $\alpha \geqslant 2$, one takes $A = 0$ and $B = \pi$ as we do in Eq. (9).

We can see that, for large values of n, i.e., at long distances, only the largest values of the cosine need to be considered in the integral. This occurs in the vicinity of A and B; we assume that the cutoff parameter which controls this approximation is k_c,

$$\begin{aligned}b_{m,n}^{(l)} \sim &\int_{A}^{A+k_c} 2\,dk(-2/\alpha)^n \cos^n(k)e^{ik(2m+n)}\\ &+ \int_{B-k_c}^{B} 2\,dk(-2/\alpha)^n \cos^n(k)e^{ik(2m+n)}.\end{aligned} \tag{A2}$$

A Taylor expansion of the cosine around points A and B yields $\cos(A+q) = \cos(A)[1 - q\,\tan(A) - q^2/2] + o(q^2)$ and $\cos(B-q) = \cos(B)[1 + q\,\tan(B) - q^2/2] + o(q^2)$. Note that the first-order terms are nonzero only for $\alpha < 2$ (for $\alpha \geqslant 2$, we have $A = 0$ and $B = \pi$), in this case, we can limit ourselves to the first-order approximation,

$$\begin{aligned}b_{m,n}^{(l)} \sim &\int_0^{k_c} 2\,dq(-1)^n e^{-n\,\tan(A)q}e^{iq(2m+n)}e^{iA(2m+n)}\\ &+ \int_0^{k_c} 2\,dq(-1)^{2n} e^{n\,\tan(B)q}e^{-iq(2m+n)}e^{iB(2m+n)}\\ \sim &\int_0^{\infty} 2\,dq(-1)^n e^{-n\,\tan(A)q}e^{iq(2m+n)}e^{iA(2m+n)}\\ &+ \int_0^{\infty} 2\,dq\, e^{-n\,\tan(A)q}e^{-iq(2m+n)}e^{iB(2m+n)}\\ \sim\ & 2(-1)^n\frac{e^{iA(2m+n)}}{\tan(A)n - i(2m+n)}\\ &+ 2\frac{e^{iB(2m+n)}}{\tan(A)n + i(2m+n)}.\end{aligned} \tag{A3}$$

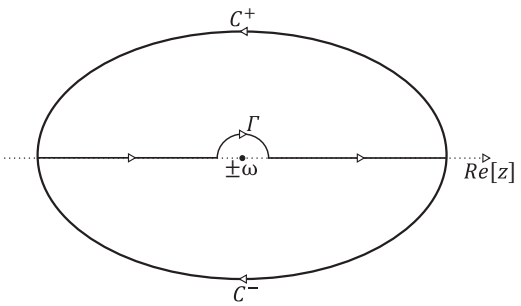

FIG. 9. Contour integral.

In the case of isotropic graphene, $A = \pi/3$. Given that $x = a_0\sqrt{3}(2m+n)/2$ and $y = -n3a_0/2$ we have

$$b(x,y)^{(l)} \sim a_0\sqrt{3}\frac{e^{i2\pi[-y+x/\sqrt{3}/(3a_0)]}}{-y-ix} + a_0\sqrt{3}\frac{e^{i4\pi x/(3\sqrt{3}a_0)}}{-y+ix}. \tag{A4}$$

One, thus, recovers the results of Ref. 14 by performing the substitution $x \to y$ and $-y \to x$.

However, for $\alpha \geqslant 2$, we have $A = 0$, the first-order terms are null, and we need to consider the second-order terms. This yields

$$\begin{aligned} b^{(l)}_{m,n} &\sim \int_0^{k_c} 2\,dq(-2/\alpha)^n e^{-n(q^2/2)}e^{iq(2m+n)} + \int_0^{k_c} 2\,dq(-2/\alpha)^n e^{-n(q^2/2)}e^{-iq(2m+n)} \\ &\sim 2(-2/\alpha)^n \exp\left[-\frac{(2m+n)^2}{2n}\right]\int_0^{\infty} dq\ \exp\left[-\frac{n}{2}\left(q + i\frac{2m+n}{n}\right)\right] \\ &\quad + 2(-2/\alpha)^n \exp\left[-\frac{(2m+n)^2}{2n}\right]\int_0^{\infty} dq\ \exp\left[-\frac{n}{2}\left(q - i\frac{2m+n}{n}\right)\right] \\ &\sim (-1)^n \frac{\exp\left[-nln\left(\frac{\alpha}{2}\right) - \frac{(2m+n)^2}{2n}\right]}{\sqrt{n}}. \end{aligned} \tag{A5}$$

This is the result presented in Eq. (9).

APPENDIX B: FRIEDEL OSCILLATIONS IN THE GAPPED PHASE

In the gapped phase, the spectrum is quadratic (although anisotropic), and the unperturbed Green's functions are proportional to the following integral:

$$I(r,\omega) = \int_{\mathbb{R}^2}\frac{d^2q}{(2\pi)^2}\frac{e^{i\vec{q}\cdot\vec{r}}}{\omega^2-q^2} = \int_0^{\infty}\frac{dq}{2\pi}\frac{q}{\omega^2-q^2}\int_0^{2\pi}\frac{d\theta}{2\pi}e^{iqr\,\cos(\theta)} = \int_0^{\infty}\frac{dq}{\pi}\frac{q}{\omega^2-q^2}\int_1^{\infty}\frac{du}{\pi}\frac{\sin(ruq)}{\sqrt{u^2-1}}, \tag{B1}$$

where $\omega > 0$ and $r = |\vec{r}|$. Partially decomposing the fraction $1/(\omega^2-q^2)$ and using the representation $1/(x+i\epsilon)$ to define the $1/x$ distribution when $\epsilon \to 0^+$ leads to

$$\begin{aligned} \int_{-\infty}^{\infty}\frac{dq}{2\pi}\frac{q\,\sin(ruq)}{\omega^2-q^2} &= \left\langle \mathrm{P}\left[\frac{1}{\omega+q}\right]\middle|\frac{1}{4\pi\omega}q\,\sin(ruq)\right\rangle + \left\langle \mathrm{P}\left[\frac{1}{\omega-q}\right]\middle|\frac{1}{4\pi\omega}q\,\sin(ruq)\right\rangle - i\pi\left\langle\delta_{-\omega}\middle|\frac{1}{4\pi\omega}q\,\sin(ruq)\right\rangle \\ &\quad - i\pi\left\langle\delta_{+\omega}\middle|\frac{1}{4\pi\omega}q\,\sin(ruq)\right\rangle \\ &= -\frac{e^{i\omega ru}}{2}. \end{aligned} \tag{B2}$$

The principal value $\mathrm{P}[1/(\omega \pm q)]$ has been determined using the contours depicted in Fig. 9. Contours C^-, C^+, and Γ give a zero contribution according to Jordan's lemma. Equivalently, one could have added an infinitely small imaginary part to $\pm\omega$ in order that these poles leave the real axis to get result (B2).

Then, the $I(r,\omega)$ integral becomes

$$I(r,\omega) = -\int_1^{\infty}\frac{du}{2\pi}\frac{e^{i\omega ru}}{\sqrt{u^2-1}} = -\frac{i}{4}H_0^{(1)}(\omega r), \tag{B3}$$

where H is a Hankel function of the first kind. Performing the linear transformation $u = it+1$, the integral reads

$$I(r,\omega) = -\frac{e^{i(\omega r+\pi/4)}}{2\pi}\int_0^{\infty} dt\,\frac{e^{-\omega rt}}{\sqrt{2t\left(1+\frac{it}{2}\right)}}, \tag{B4}$$

which is the Laplace transform of $[2t(1+\frac{it}{2})]^{1/2}$. Thanks to the Watson lemma, a series expansion of this term leads to

$$\begin{aligned} I(r,\omega) &= -\frac{e^{i(\omega r+\pi/4)}}{2\pi}\sum_{k=0}^{\infty}\frac{i^k}{2^{k+1/2}}\frac{\Gamma\left(\frac{1}{2}\right)}{k!\Gamma\left(\frac{1}{2}-k\right)} \\ &\quad\times\int_0^{\infty} dt\,e^{-\omega rt}t^{k-1/2} \\ &= -\frac{e^{i(\omega r+\pi/4)}}{2\pi}\sum_{k=0}^{\infty}\frac{i^k}{2^{k+1/2}}\frac{\Gamma\left(\frac{1}{2}\right)}{k!\Gamma\left(\frac{1}{2}-k\right)} \\ &\quad\times\int_0^{\infty}\frac{dt}{\omega r}e^{-t}\left(\frac{t}{\omega r}\right)^{k+1/2-1} \\ &= -\frac{e^{i(\omega r+\pi/4)}}{2\pi}\sum_{k=0}^{\infty}\frac{i^k}{2^{k+1/2}}\frac{\Gamma\left(\frac{1}{2}\right)}{k!\Gamma\left(\frac{1}{2}-k\right)}\frac{\Gamma\left(\frac{1}{2}+k\right)}{(\omega r)^{k+1/2}} \\ I(r,\omega) &= -\frac{e^{i(\omega r+\pi/4)}}{2\sqrt{2\pi\omega r}}\sum_{k=0}^{\infty}\frac{\Gamma\left(\frac{1}{2}+k\right)}{k!\Gamma\left(\frac{1}{2}-k\right)}\left(\frac{i}{2\omega r}\right)^k. \end{aligned} \tag{B5}$$

[1]V. M. Pereira, A. H. Castro Neto, and N. M. R. Peres, Phys. Rev. B **80**, 045401 (2009).
[2]J. M. B. Lopes dos Santos, N. M. R. Peres, and A. H. Castro Neto, Phys. Rev. Lett. **99**, 256802 (2007).
[3]R. de Gail, M. O. Goerbig, F. Guinea, G. Montambaux, and A. H. Castro Neto, Phys. Rev. B **84**, 045436 (2011).
[4]C. L. Kane and E. J. Mele, Phys. Rev. Lett. **95**, 226801 (2005).
[5]T. Fukui and Y. Hatsugai, Phys. Rev. B **75**, 121403(R) (2007).
[6]Q.-f. Sun and X. C. Xie, Phys. Rev. Lett. **104**, 066805 (2010).
[7]C. Weeks, J. Hu, J. Alicea, M. Franz, and R. Wu, Phys. Rev. X **1**, 021001 (2011).
[8]N. Levy, S. A. Burke, K. L. Meaker, M. Panlasigui, A. Zettl, F. Guinea, A. H. C. Neto, and M. F. Crommie, Science **329**, 544 (2010).
[9]F. Guinea, M. I. Katsnelson, and A. K. Geim, Nat. Phys. **6**, 30 (2010).
[10]L. Tarruell, D. Greif, T. Uehlinger, G. Jotzu, and T. Esslinger, Nature (London) **483**, 302 (2012).
[11]G. Montambaux, F. Piéchon, J.-N. Fuchs, and M. O. Goerbig, Phys. Rev. B **80**, 153412 (2009).
[12]Y. Hasegawa, R. Konno, H. Nakano, and M. Kohmoto, Phys. Rev. B **74**, 033413 (2006).
[13]K. K. Gomes, W. Mar, W. Ko, F. Guinea, and H. C. Manoharan, Nature (London) **483**, 306 (2012).
[14]V. M. Pereira, F. Guinea, J. M. B. Lopes dos Santos, N. M. R. Peres, and A. H. Castro Neto, Phys. Rev. Lett. **96**, 036801 (2006).
[15]N. M. R. Peres, F. Guinea, and A. H. Castro Neto, Phys. Rev. B **73**, 125411 (2006).
[16]T. O. Wehling, A. V. Balatsky, M. I. Katsnelson, A. I. Lichtenstein, K. Scharnberg, and R. Wiesendanger, Phys. Rev. B **75**, 125425 (2007).
[17]V. V. Cheianov and V. I. Fal'ko, Phys. Rev. Lett. **97**, 226801 (2006).
[18]E. Mariani, L. I. Glazman, A. Kamenev, and F. von Oppen, Phys. Rev. B **76**, 165402 (2007).
[19]C. Bena, Phys. Rev. Lett. **100**, 076601 (2008).
[20]B. Sutherland, Phys. Rev. B **34**, 5208 (1986).
[21]M. Inui, S. A. Trugman, and E. Abrahams, Phys. Rev. B **49**, 3190 (1994).
[22]P. W. Brouwer, E. Racine, A. Furusaki, Y. Hatsugai, Y. Morita, and C. Mudry, Phys. Rev. B **66**, 014204 (2002).
[23]V. M. Pereira, J. M. B. Lopes dos Santos, and A. H. Castro Neto, Phys. Rev. B **77**, 115109 (2008).
[24]M. Fujita, K. Wakabayashi, K. Nakada, and K. Kusakabe, J. Phys. Soc. Jpn. **65**, 1920 (1996).
[25]K. Nakada, M. Fujita, G. Dresselhaus, and M. S. Dresselhaus, Phys. Rev. B **54**, 17954 (1996).
[26]C. Bena and G. Montambaux, New J. Phys. **11**, 095003 (2009).